Numerical Investigation of Hypervelocity Shock-Wave/Boundary-Layer Interactions over a Double-Wedge Configuration

Jiaao Hao[a], Chih-Yung Wen[a,*], Jingying Wang[b]

[a] Department of Mechanical Engineering, The Hong Kong Polytechnic University, Kowloon, Hong Kong

[b] School of Energy and Power Engineering, Shandong University, Jinan, Shandong, 250100, China

Abstract

Hypervelocity flows of nitrogen and air over a 30°-55° double-wedge configuration are numerically investigated under the condition corresponding to recent experiments conducted with total enthalpy of 8.0 MJ/kg. Time-accurate two-dimensional and three-dimensional simulations are performed to resolve the unsteady shock interaction process. For the nitrogen flow, it is found that the three-dimensional simulation predicts a much smaller separation bubble and reduced surface heat flux and pressure peaks. Good agreement can be observed with the experiments in terms of the shock location, the flow structure, and the time-averaged surface heat flux when the three-dimensional effects are considered. For the air flow, the shock interaction mechanisms are similar to those in nitrogen. The real-gas effects tend to decrease the separation bubble and reduce the standoff distance of the detached shock induced by the second wedge, leading to a lower surface heat flux peak compared with the nitrogen result. However, the trend of the experimental heat flux data shows the opposite. To explain the discrepancies, effects of thermochemical nonequilibrium models are investigated. The results indicate that the air flow under the current condition is insensitive to air chemistry and vibration–dissociation coupling models. Suggestions for further study are presented.

Keywords: hypersonic; thermochemical nonequilibrium; vibration–dissociation

---

[*]Corresponding author
  Email address: cywen@polyu.edu.hk

coupling; shock-wave/boundary-layer interaction

1 Introduction

Hypervelocity flow is conventionally defined as the flow regime where the Mach number is larger than five and the flow total enthalpy is of the order of gas dissociation energy [1]. Different from the "cold" hypersonic flow (where the speed of sound is reduced to achieve hypersonic but the flow total enthalpy is not enough to excite the thermochemical nonequilibrium processes), its characteristics are much more complex than a direct extension of supersonic aerodynamics. The high-speed freestream is compressed by a strong shock wave resulting in an extremely high translational temperature. On the one hand, the internal energy modes of the fluid are excited accompanied by thermal nonequilibrium due to the relatively low collision frequency. Chemical reactions, on the other hand, would occur between reactive species including dissociation, neutral exchange, and ionization. Such thermochemical nonequilibrium processes, also known as the real-gas effects, could have a significant impact on the performance of hypersonic vehicles such as the anomaly of the Space Shuttle flaps [2,3].

During hypersonic flights, shock-wave/boundary-layer interaction (SWBLI) is an important flow phenomenon, which could be effectively studied with canonical configurations including compression corners, shock impingement on flat plates, double wedges, and double cones. Among these geometries, the flow characteristics over double-wedge and double-cone configurations are known to be sensitive to thermochemical nonequilibrium models, which makes them ideal benchmarks to understand real-gas effects on SWBLI and to validate related physical models. However, it was found that the frozen vibrational energy and chemical compositions in the freestream of reflected shock tunnels could affect the shock standoff distances and surface heat fluxes significantly [4–7]. Therefore, the source of any discrepancies between numerical predictions and measurements cannot be easily interpreted. There is currently a lack of experimental data obtained under the condition where a clean freestream (in thermochemical equilibrium state) with high enthalpy is provided.

In 2012, Swantek and Austin [8] conducted a set of double-wedge experiments in

the Hypervelocity Expansion Tube at the University of Illinois Urbana-Champaign with total enthalpies ranging from 2.1 to 8.0 MJ/kg in nitrogen and air. Time-averaged surface heat flux data and schlieren images were obtained. Significant differences in the surface heat flux distributions and flow behaviors were observed between the nitrogen and air flows at total enthalpy of 8.0 MJ/kg, which was attributed to real-gas effects.

To assess the prediction capability of computational fluid dynamics (CFD) tools for hypersonic SWBLI, researchers have compared their numerical results with the measurements of Swantek and Austin [8]. Durna et al. [9] performed a time-accurate two-dimensional (2-D) simulation of the nitrogen flow case at 2.1 MJ/kg. The time-averaged surface heat flux distribution was in good agreement with the experimental data, whereas the predicted instantaneous flow structures were evidently different from the schlieren photographs. Komives et al. [10] and Reinert et al. [11] simulated the nitrogen flow cases with total enthalpies of 2.1 and 8.0 MJ/kg. It was indicated that the three-dimensional (3-D) predictions matched the experimental data better than the 2-D results. However, the time accuracy in their simulations might not be enough. Tumuklu et al. [12] numerically investigated the nitrogen and air flows at 8.0 MJ/kg using the direct simulation Monte Carlo method and found that the locations of the triple points showed closer agreement with the measurements when 3-D effects were considered for the nitrogen flow. In contrast, good agreement could be obtained with the 2-D simulation for the air flow due to the fact that chemical reactions reduce the spanwise flow and the size of the separation region and lead to the reduction of 3-D effects. However, time-averaged surface heat fluxes were not provided, and thus a direct comparison with the experimental data could not be made. Knight et al. [13] compared various numerical results evaluated by several research organizations and emphasized the importance of fully 3-D simulation for the nitrogen flow. It was also found that there were large discrepancies between numerical and experimental surface heat fluxes for the air flow and the causes are yet to be investigated.

It is the objective of the current study to extend the previous studies to a time-accurate 3-D computation with the surface heat fluxes averaged over an appropriate

interval for the nitrogen flow at 8.0 MJ/kg. Sharing the same concerns with Kianvashrad and Knight [14] on hypersonic hollow-cylinder-flare flows, this study also aims to reveal to what extent the experiment in air represents a test of nonequilibrium effects given that the total enthalpy is commonly considered to be moderate. Time-accurate 2-D simulations are therefore performed for the air flow at 8.0 MJ/kg with different thermochemical nonequilibrium models to explain the large discrepancies between CFD and experiments. In the remainder of the paper, the geometric configuration and the flow conditions are presented in Section 2, followed by a description of the physical models and numerical methods in Section 3. In Section 4, an independence study is conducted to determine the appropriate grid resolution and timestep. Shock interaction mechanisms are then presented, and numerical results are compared with the experiments for the nitrogen and air flows in Sections 5 and 6. In Section 6, effects of thermochemical nonequilibrium models are also discussed together with a preliminary study to demonstrate the influence of possible laminar-turbulent transition. Finally, conclusions are given in Section 7.

2 Geometric configuration and flow conditions

The double-wedge configuration, as shown in Fig. 1, has two sections with half-angles of 30° and 55°. The surface lengths of the forward and aft sections (L_1 and L_2) are 50.8 and 25.4 mm, respectively. The width of the double wedge is 101.6 mm. The coordinate system is constructed with the origin located at the nose of the first wedge on the midspan plane, the x axis pointing in the horizontal direction, the y axis pointing in the vertical direction, and the z axis completing the right-handed system.
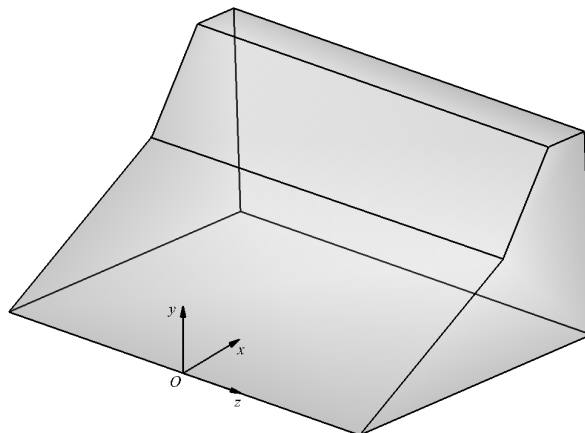
Fig. 1. Schematic of the Double-wedge configuration.

The flow conditions are listed in Table 1. The difference on the freestream parameters between the nitrogen and air flows was found to be less than 0.5% [8], which is therefore neglected here. In the table, the characteristic time τ_c is defined by $\tau_c \equiv L_c/U_\infty$. The test time τ_t corresponds to approximately 15.4 τ_c. The Reynolds number based on the characteristic length of the model is 2.61×10^4, and thus the flow is assumed to be laminar. However, local laminar-turbulent transition due to the existence of shear layers could occur, the effects of which will be examined later with Reynolds-averaged Navier–Stokes (RANS) simulations.

During the experiments of Swantek and Austin [8], Schlieren images at different instants were obtained. Surface heat flux data collected by each gauge were averaged for an interval from the establishment time to τ_t. Note that the heat transfer establishment time is defined as the time for the heat transfer to reach the mean of the established value. Strictly speaking, the simulated surface heat flux should be averaged using the same time interval as the experiments for each gauge. However, given that modeling of the tunnel start-up process is beyond the scope of this study, all the time-averaged results are evaluated using the triple point establishment time (100 μs for the nitrogen flow and 80 μs for the oxygen flow), which could agree well with the heat transfer establish times near shock impingement and peak heating [15].

Table 1. Flow conditions [8].

Flow parameter	Value
Mach number, M_∞	7.14
Stagnation enthalpy, h_0 (MJ/kg)	8.0
Static temperature, T_∞ (K)	710
Static pressure, p_∞ (kPa)	0.780
Velocity, U_∞ (m/s)	3812
Density, ρ_∞ (kg/m³)	0.0038
Unit Reynolds number, Re_∞ (m^{-1})	4.35×10^5
Characteristic length, L_c (mm)	60

| Characteristic time, τ_c (µs) | 15.7 |
| Test time, τ_t (µs) | 242 |

3 Physical models and numerical methods

Under the two-temperature assumption, the translational–rotational energy mode is fully excited in terms of a translational–rotational temperature T_{tr}, and the vibrational energy of molecules and the electronic excitation energy are in equilibrium corresponding to a vibrational–electronic temperature T_{ve}. The hypersonic thermochemical nonequilibrium flow over the double-wedge configuration is governed by the conservation equations of species mass, mixture momentum, total energy, and total vibrational–electronic energy. The governing equations can be written in the following vector form:

$$\int_V \frac{\partial \boldsymbol{U}}{\partial t} dV + \int_S \left(\boldsymbol{F} - \boldsymbol{F}_v \right) \cdot \boldsymbol{n} dS = \int_V \boldsymbol{\Omega} dV \,, \tag{1}$$

where $\boldsymbol{U} = (\rho_i, \rho u, \rho v, \rho w, \rho e, \rho e_{\text{ve}})^{\text{T}}$ is the vector of conservative variables, $\boldsymbol{F}$ is the vector of inviscid fluxes, $\boldsymbol{F}_v$ is the vector of viscous fluxes, and $\boldsymbol{\Omega} = (\omega_i, 0, 0, 0, 0, \omega_{\text{ve}})^{\text{T}}$ is the vector of source terms. In these expressions, ρ_i is the density of species i, ρ is the density of the mixture, u, v, and w are the velocities in the x, y, and z directions, respectively, p is the pressure, e is the specific total energy of the mixture, e_{ve} is the specific vibrational–electronic energy of the mixture, and ω_i and ω_{ve} represent the production rates of species mass and the vibrational–electronic energy per unit volume, respectively. The equation of state is represented by the Dalton's law of partial pressures and the perfect gas law for each species.

The harmonic oscillator model is used to evaluate the vibrational energy, and only the first two levels are considered for the electronic energy. Based on the law of mass reaction, ω_i can be expressed as

$$\omega_i = M_i \sum_{r=1}^{nr} \left(\beta_{r,i} - \alpha_{r,i} \right) \left(k_{f,r} \prod_{j=1}^{ns} \left(\frac{\rho_j}{M_j} \right)^{\alpha_{r,j}} - k_{b,r} \prod_{j=1}^{ns} \left(\frac{\rho_j}{M_j} \right)^{\beta_{r,i}} \right), \tag{2}$$

where nr denotes the total number of reactions, ns denotes the total number of species, M_i is the species molecular mass, $\alpha_{r,i}$ and $\beta_{r,i}$ are the stoichiometric coefficients for

reactants and products, respectively, and $k_{f,r}$ and $k_{b,r}$ are the forward and backward reaction rate coefficients, which can be expressed as

$$k_{f,r} = Zk_{f,eq,r} \quad \text{and} \quad k_{b,r} = \frac{k_{f,eq,r}}{K_{eq,r}}. \tag{3}$$

In these expressions, Z is the nonequilibrium factor, $k_{f,eq,r}$ is the equilibrium rate coefficient, and $K_{eq,r}$ is the equilibrium constant. $k_{f,eq,r}$ can be expressed in the modified Arrhenius form as

$$k_{f,eq,r} = A_r T_{tr}^{B_r} \exp\left(-C_r/T_{tr}\right), \tag{4}$$

where A_r, B_r, and C_r are the reaction parameters.

The term ω_{ve} can be further decomposed into two parts as

$$\omega_{ve} = \omega_{t-v} + \omega_{chem,v}, \tag{5}$$

where ω_{t-v} represents the energy transfer between the translational mode of heavy particles and the vibrational mode of molecules, and $\omega_{chem,v}$ represents the added or removed vibrational energy due to recombination and dissociation.

3.1 Physical models

Two thermochemical nonequilibrium schemes are considered in this study. For the baseline scheme, Park's 1990 chemical reaction model [16] is employed to calculate the equilibrium rate coefficients. Due to the negligible degree of ionization in the cases under investigation, only the reactions involving the neutral species (N, O, N_2, O_2, NO) are considered. ω_{t-v} is modeled using the Landau–Teller model [17], where the vibrational relaxation times are calculated via the Millikan–White expression [18] with the parameters given by Hash et al. [19]. Park's correction [16] is introduced to avoid the underprediction of the relaxation times at high temperatures. To account for the vibration–dissociation coupling effects, Z is defined by

$$Z_{Baseline} = \left(\frac{T_{c,r}}{T_{tr}}\right)^{n_r} \exp\left(\frac{C_r}{T_{tr}} - \frac{C_r}{T_{c,r}}\right), \tag{6}$$

where n_r and C_r are the reaction parameters of the r-th reaction, and $T_{c,r}$ is the controlling temperature, which is set to the geometric average of T_{tr} and T_{ve} with half power for dissociation reactions induced by heavy particle impacts and T_{tr} for neutral

exchange reactions, respectively. The nonpreferential model [20] is employed to evaluate $\omega_{\text{chem,v}}$, which means that molecules are created or destroyed at the average vibrational energy. All the simulations in this paper are performed using the baseline scheme unless otherwise stated.

The second thermochemical nonequilibrium scheme (the improved scheme) upgrades Park's 1990 chemical reaction model with new reaction parameters for the dissociation reactions of O_2 induced by O, N_2, and O_2 impacts, while the parameters for the dissociation reactions of N_2 and NO and the neutral exchange reactions remain unchanged. All the new reaction parameters, as listed in Table 2, are taken from available quasi-classical trajectory (QCT) calculations in the literature [21–23]. The coupled vibration-dissociation-vibration (CVDV) model [24] is used to model the vibration–dissociation coupling effects, which assumes that truncated harmonic oscillators relax through Boltzmann distributions corresponding to T_{ve} and that the probabilities of dissociation scale exponentially with vibrational levels. The resulting Z_{CVDV} can be evaluated from

$$Z_{\text{CVDV}} = \frac{Q_{\text{v}}(T_{\text{tr}})Q_{\text{v}}(T_F)}{Q_{\text{v}}(T_{\text{ve}})Q_{\text{v}}(-U)}, \tag{7}$$

where Q_{v} is the vibrational partition function, and T_F is defined by

$$\frac{1}{T_F} = \frac{1}{T_{\text{ve}}} - \frac{1}{T_{\text{tr}}} - \frac{1}{U} \tag{8}$$

with U being a parameter in the unit of temperature. The term $\omega_{\text{chem,v}}$ can be obtained by

$$\omega_{\text{chem,v}} = \sum_{s=mol.} \omega_{b,s}\bar{E}_s(-U) - \omega_{f,s}\bar{E}_s(T_F), \tag{9}$$

where $\omega_{f,s}$ and $\omega_{b,s}$ are the forward and backward rates of the molecular number density production per unit volume, respectively, and the function of weighted average vibrational energy is defined by

$$\bar{E}_s(T) = \frac{k\theta_{\text{v},s}}{\exp(\theta_{\text{v},s}/T)-1} - \frac{k\theta_{\text{d},s}}{\exp(\theta_{\text{d},s}/T)-1}. \tag{10}$$

In this expression, $\theta_{\text{v},s}$ and $\theta_{\text{d},s}$ denote the characteristic vibrational temperature and

dissociation temperature of species s, respectively. Based on the comparison with the state-specific data obtained using the forced harmonic oscillator model and the QCT method, the semi-empirical parameter U is set to $\theta_d/6$ for N_2 as recommended by Lino da Silva et al. [25], while $\theta_d/3$ is suggested for O_2 by Hao et al. [26].

Table 2. Reaction parameters for dissociation reactions of O_2 in the improved scheme.

Reaction	Third particle	A (cm^3/mol/s)	B	C (K)
	O	1.725×10^{18}	-0.4037	60,540
$O_2 + M \leftrightarrow 2O + M$	N_2	4.897×10^{15}	-0.1310	59,380
	O_2	1.483×10^{20}	-1.0495	62,720

The viscous stresses are modeled based on Newtonian fluid with Stokes' hypothesis. Heat fluxes are calculated using Fourier's law for all energy modes. The species mass diffusion fluxes are modeled according to the modified Fick's law [27] to ensure the zero-sum of diffusion fluxes. Transport properties of the gas mixture are calculated using Gupta's mixing rule [28] with the collision integrals data given by Wright et al. [29].

3.2 Numerical methods

The numerical simulations in this study are performed using a multi-block parallel finite-volume CFD code called PHAROS [30,31], which has been successfully applied to thermochemical nonequilibrium flows over double-cone and hollow-cylinder/flare configurations [32–35]. The inviscid fluxes are calculated using the modified Steger–Warming scheme [36], which can capture strong shocks stably while maintaining sufficient viscous resolution. The scheme is then extended to higher order by the monotone upstream-centered schemes for conservation laws (MUSCL) reconstruction [37] with the van Leer slope limiter [38]. The viscous fluxes are calculated using a second-order central difference. A second-order implicit point relaxation method [39] is used for time marching, which is equivalent to the Crank–Nicolson method in the domain where the local CFL numbers are less than one and switches to the backward Euler method elsewhere.

4 Computational details

In this section, the gird size for the 2-D simulations is firstly determined under the

air flow condition with three levels of grid refinement: 512 × 256 (coarse), 768 × 384 (medium), and 1024 × 512 (fine). All the grids are constructed with the normal spacing of 1×10^{-7} m on the body surface to ensure that the grid Reynolds number Re_w is on the order of magnitude of one. Details of the coarse grid are illustrated in Fig. 2. As can be seen, the grid in the vicinity of the hinge has been carefully designed so that the grid spacing could vary smoothly in the interior of the domain.
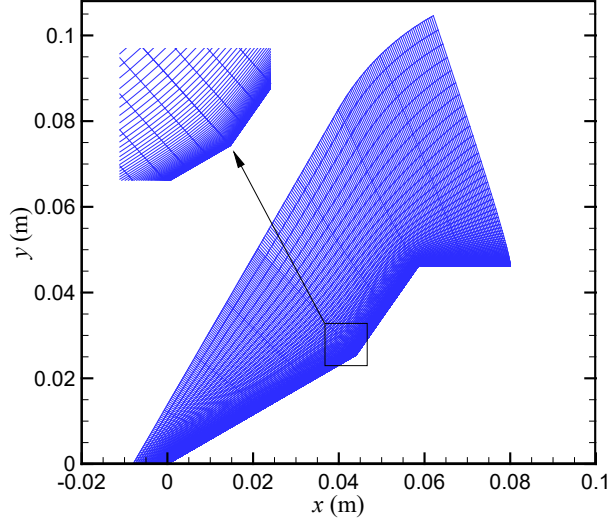
Fig. 2. Computational grid for the 2-D simulations (coarse grid with every other node).

The boundary conditions for the 2-D simulations are specified as follows: The freestream condition given in Table 1 is set on the inflow boundary; first-order extrapolation is applied for the outflow boundary; no-slip condition together with a fixed wall temperature of 298 K are implemented on the double-wedge surface. The isothermal wall assumption is used because the wall temperature of the model remains nearly constant in the experiments due to the very short run times of the tunnel. In addition, the surface is assumed to be noncatalytic.

At this step, simulations are performed with a constant Courant–Friedrichs–Lewy (CFL) number of 10,000 for all the grid levels. After 3000 iterations corresponding to approximately 1000 flow times, the steady-state solution is obtained with a ten order of magnitude reduction in the L_2 norm density residual. The steady-state distributions of surface heat flux predicted on different grids are compared in Fig. 3. The surface heat flux is computed using

$$q_w = k_{tr} \left. \frac{\partial T_{tr}}{\partial n} \right|_w + k_{ve} \left. \frac{\partial T_{ve}}{\partial n} \right|_w , \tag{11}$$

where k_{tr} and k_{ve} are the translational–rotational and vibrational–electronic conductivities at the wall, respectively. Note that the flux corresponding to chemical diffusion is zero due to the noncatalytic condition. It is shown that the size of the separation region is significantly underpredicted using the coarse grid. As the grid refines, the separation zone increases and approaches to a certain level. Based on the observation that the distributions obtained using the medium and fine grids are almost identical, the medium grid should be adequate to ensure grid independence for the 2-D simulations.
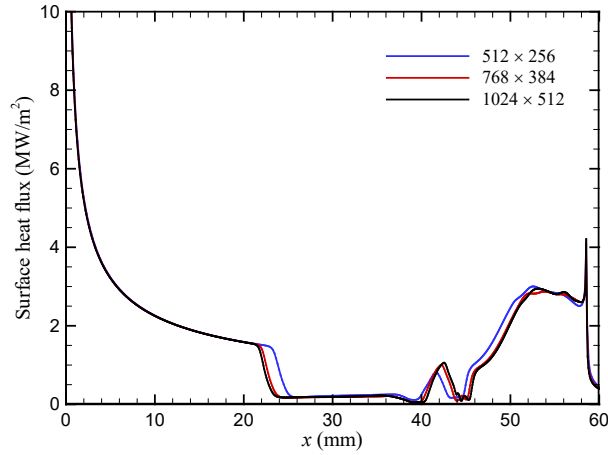
Fig. 3. Steady-state distributions of surface heat flux predicted on different 2-D grids in air.

For simulations of hypersonic SWBLI, the timestep used in an explicit time integration would be extremely small as a result of the highly stretched grid near the surface and the restriction of stability condition, leading to a large number of iterations. To reduce computational cost, an implicit time integration scheme is employed in this study. However, the timestep used in the implicit simulations must be carefully selected to maintain enough time accuracy. It is important to note that all the unsteady simulations in this study are initialized using the freestream values everywhere in the flowfields.

Following the 2-D grid independence study, unsteady simulations are performed on the medium grid for the air flow with $\Delta t = 1$, 5 and 10 ns. For these timesteps, the local CFL numbers are kept less than unity in the interior of the domain, while the

largest local CFL numbers located on the surface correspond to 3.8, 19.0, and 38.0, respectively. The time-averaged distributions of surface heat flux for an interval from t = 80 to 242 μs are displayed in Fig. 4. It is indicated that Δt = 5 ns would be adequate for the 2-D unsteady simulations.
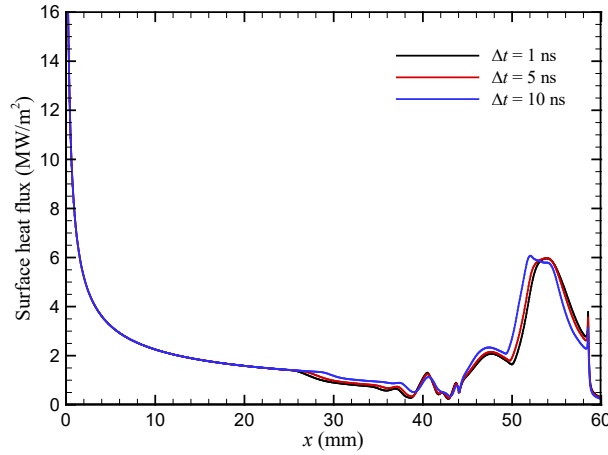

Fig. 4. Time-averaged distributions of surface heat flux predicted on the medium grid with different Δt in air.

Finally, the grid size along the model in the spanwise direction is determined for the 3-D simulation. Two grids are constructed with 70 and 170 nodes in the spanwise direction, respectively, while the nodes in streamwise and wall-normal directions are the same with the medium grid for the 2-D simulations. Unsteady simulations are performed for the nitrogen flow with Δt = 5 ns on the two grids. Note that the average spanwise spacing for the fine grid is 0.68 mm so that the local CFL numbers in the interior of the domain are still less than unity. Figure 5 shows the time-averaged distributions of surface heat flux along the centerline for an interval from t = 100 to 242 μs. It can be seen that 70 nodes in the spanwise direction should be fine enough for the 3-D simulation, despite some difference near x = 38 mm.
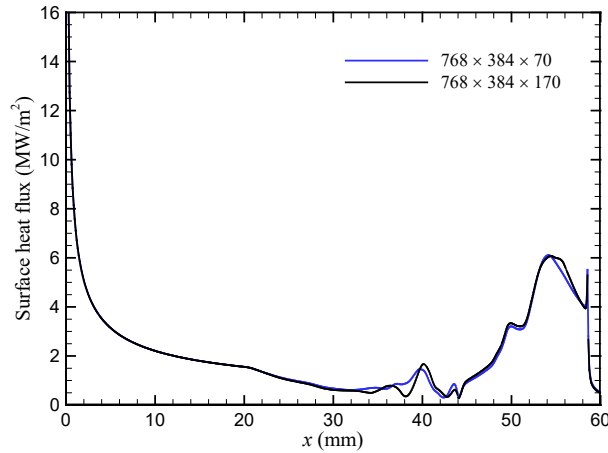
Fig. 5. Time-averaged distributions of surface heat flux along the centerline predicted on different 3-D grids in nitrogen.

5 Results and discussion: nitrogen flow

5.1 Shock interaction mechanisms

To demonstrate the flow mechanisms of SWBLI, contours of the density gradient magnitude obtained from the 2-D simulation are displayed in Fig. 6 at $t = 60, 120, 180,$ and 242 μs for the nitrogen flow. The general features of the shock interaction can be described as follows: An attached shock (AS) wave generated by the first wedge interacts with the detached shock (DS) wave by the second wedge at the triple point (TP) to form a transmitted shock (TS) and a slip line (SL). The TS impinges on the surface and creates a strong adverse pressure gradient, which feeds upstream through the subsonic portion of the boundary layer and results in a large-scale flow separation region. However, the flow details may vary, when the flowfields are examined closely at different instants.

At $t = 60$ μs, the AS and DS have basically established, whereas the separation region in the vicinity of the hinge is still evolving at an early stage. Due to the relatively small separation bubble, both the induced separation and reattachment shocks (SS_1 and RS_1) interact with the transmitted shock. There is another small separation bubble near the impingement point of the TS, which generates a pair of separation and reattachment shocks (SS_2 and RS_2) in addition to those described above. Edney's type II shock interference [40] occurs between the TS and SS_2, resulting in a Mach stem (MS), a pair of triple points, and two new transmitted shocks. Behind the Mach stem, a diamond

13

shaped subsonic pocket is formed. The subsonic flow then accelerates to supersonic speed driven by the converging-diverging flow path confined between the SL and the second wedge, as reported by Durna et al. [9].

At $t = 120$ μs, the separation region has grown much larger so that the induced separation shock SS_1 joins the AS instead of interacting with the TS. Since the standoff distance of the detached shock also becomes larger, the primary TP moves upstream. As seen in Fig. 6(b), several weak separation shocks are produced by the secondary separation bubbles in the separation region. The Mach stem and the subsonic region disappear. Instead, the multiple shocks are reflected by the SL and the wedge surface and intersect each other regularly.

From $t = 120$ to 242 μs, the basic flow patterns remain similar. As the separation bubble keeps growing, the separation shock moves upstream, while the reattachment shock moves downstream. However, the stand-off distance of the DS has shown little change since $t = 120$ μs. As a result, the primary TP has moved farther away from the wedge surface and slightly downstream during this time period. It is also found that the 2-D simulation has not reached steady state at $t = 242$ μs.

(a) $t = 60$ μs   (b) $t = 120$ μs

(c) $t = 180$ μs   (d) $t = 242$ μs
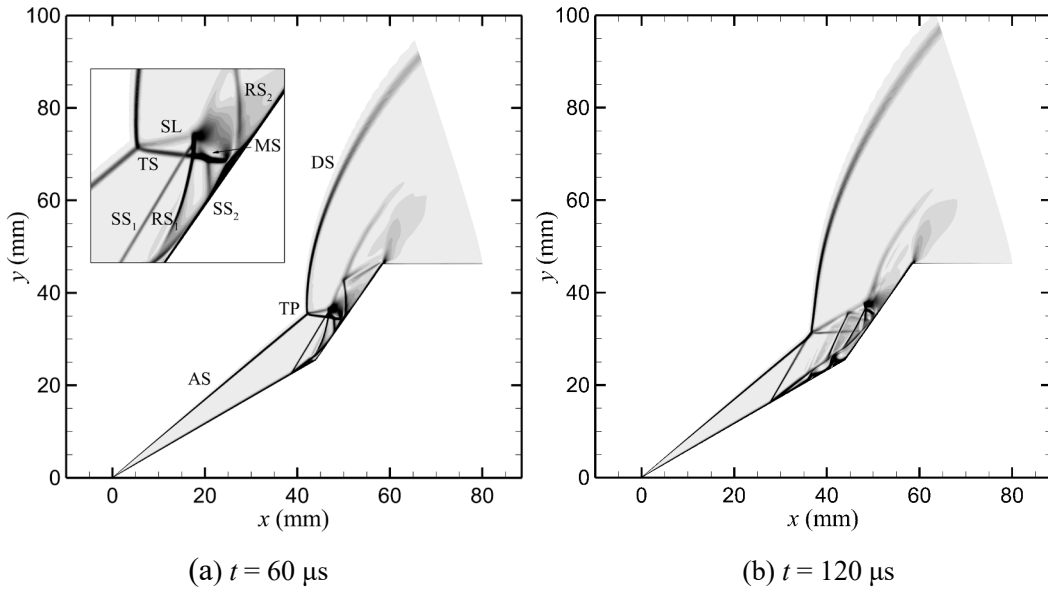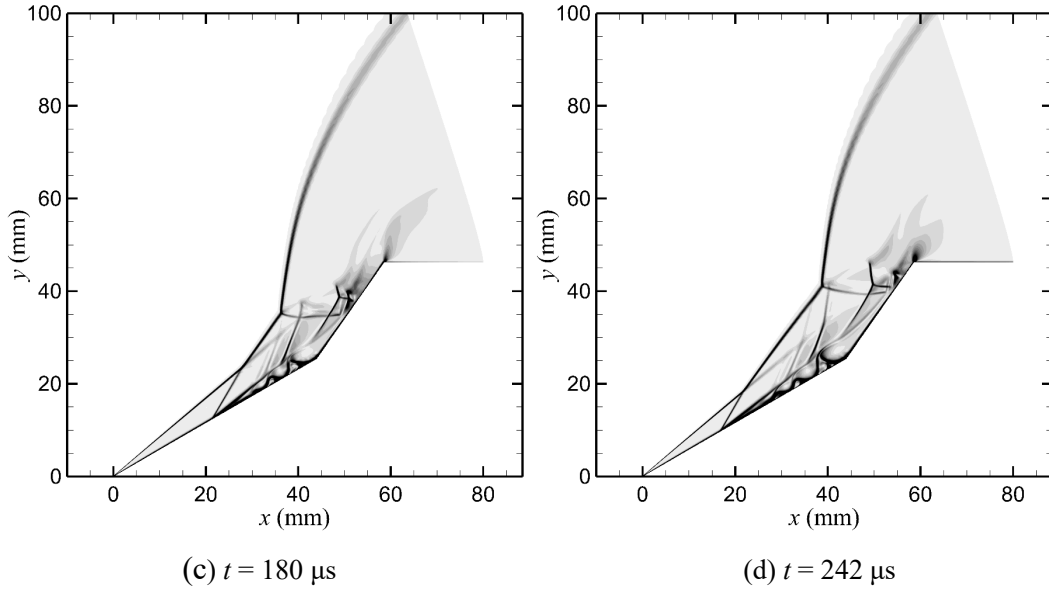
Fig. 6. Contours of the density gradient magnitude obtained from the 2-D simulation at different instants in nitrogen.

The shock interaction mechanisms obtained from the 3-D simulation, as illustrated in Fig. 7, are almost identical to those from the 2-D simulation at different instants. However, the size of the separation and the standoff distance of the detached shock are smaller, which could be attributed to the 3-D relieving effect. Edney's type II shock interference instead of type I takes place between the TS and the reattachment shock due to the change of the shock strength at $t = 242$ μs. Compared with the 2-D results, the location of the separation point moves downstream due to the shrink of the separation bubble. However, since the DS lies much closer to the surface, the primary TP moves even more downstream regardless of the reduced separation bubble. At $t = 242$ μs, the impingement point of TS has become very close to the expansion corner.

(a) $t = 60$ μs   (b) $t = 120$ μs

(c) $t = 180$ μs   (d) $t = 242$ μs
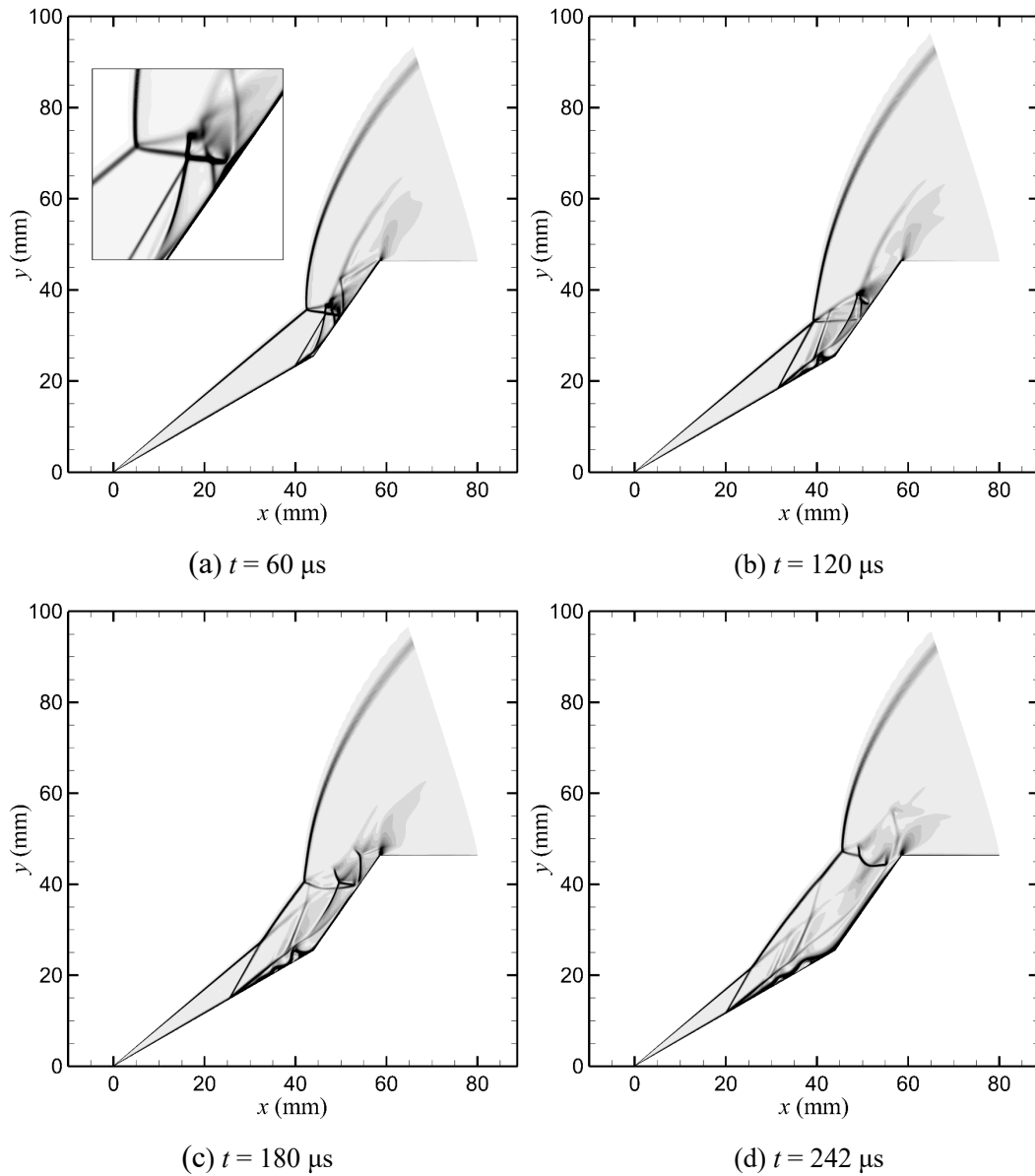
Fig. 7. Contours of the density gradient magnitude at the midspan obtained from the 3-D simulation at different instants in nitrogen.

Figure 8 depicts the streamlines and the contours of pressure on the surface obtained from the 3-D simulation at different instants. Note that only the top view of the double wedge near the midspan is displayed. There is no obvious spanwise flow at $t = 60$ and 120 μs, whereas 3-D effects become apparent at $t = 180$ and 242 μs. Multiple separation and reattachment lines can be observed at the end of the test time, indicating that there exist several small bubbles in the primary separation region.

16
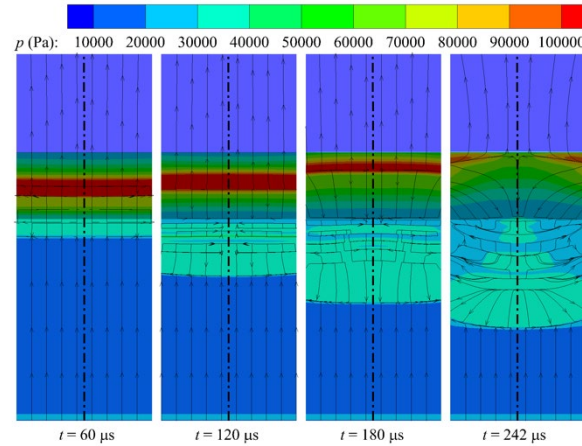
Fig. 8 Surface streamlines and contours of pressure at different instants.

Figures 9–11 present the simulated evolutions of surface skin friction, heat flux, and pressure, respectively. Flow separation and reattachment occur at the locations where skin friction equals zero. The sudden sink of heat flux and the increase in pressure on the first wedge indicate the separation of the boundary layer, and the peaks are caused by the flow reattachment and the shock impingement on the second wedge. It is clear that as the flow develops, the separation point moves upstream, whereas the locations of the heat flux and pressure peaks move downstream. However, there is no evident change in the peak values from $t = 60$ to 242 μs except that the peak pressure predicted by the 3-D simulation at $t = 242$ μs is significantly reduced by the expansion waves centered at the corner. Spatial oscillations induced by the secondary separation bubbles can be observed in the separation region after $t = 120$ μs. Compared with the 2-D results, the 3-D distributions show smaller separation regions and substantially lower peak values. Different from the scenario of cylinders and spheres, 3-D relieving effects result in a decrease in surface heat flux instead of an enhance. This is because the weaker shock interaction predicted by the 3-D simulation dominates the flowfields.
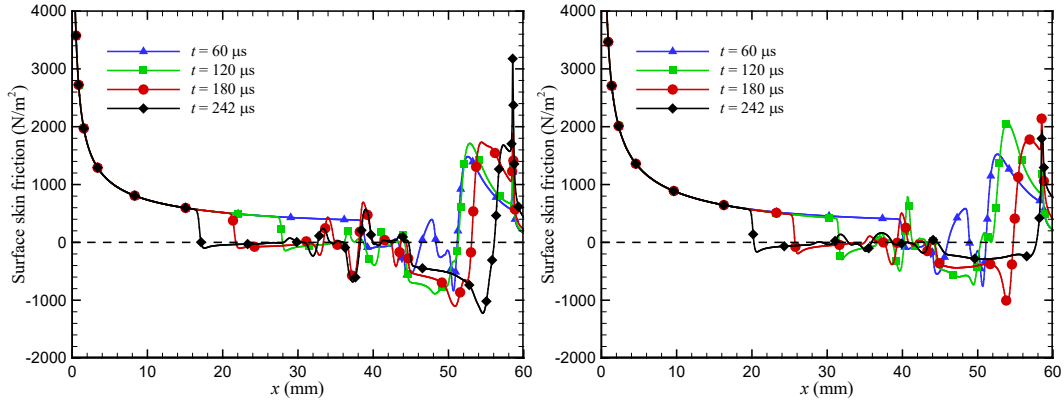
Fig. 9. Evolutions of surface skin friction obtained from the 2-D (left) and 3-D (right)

simulations in nitrogen.
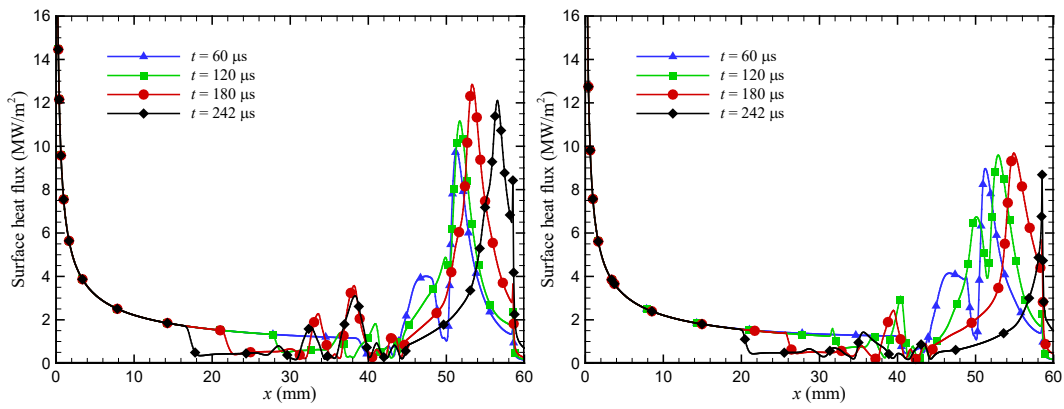
Fig. 10. Evolutions of surface heat flux obtained from the 2-D (left) and 3-D (right)

simulations in nitrogen.
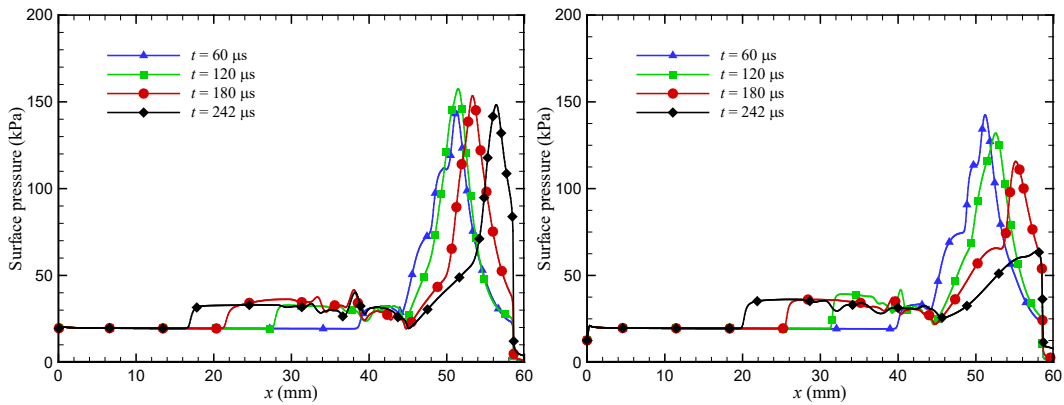
Fig. 11. Evolutions of surface pressure obtained from the 2-D (left) and 3-D (right)

simulations in nitrogen.

5.2 Comparison with experiments

Figure 12 presents the experimental and simulated shock shapes at different instants. The standoff distance of the detached shock is smaller, and the triple point is more shifted downstream when 3-D effects are considered, better matching the

18

experiment.

(a) $t = 100$ μs

(b) $t = 160$ μs

(c) $t = 200$ μs
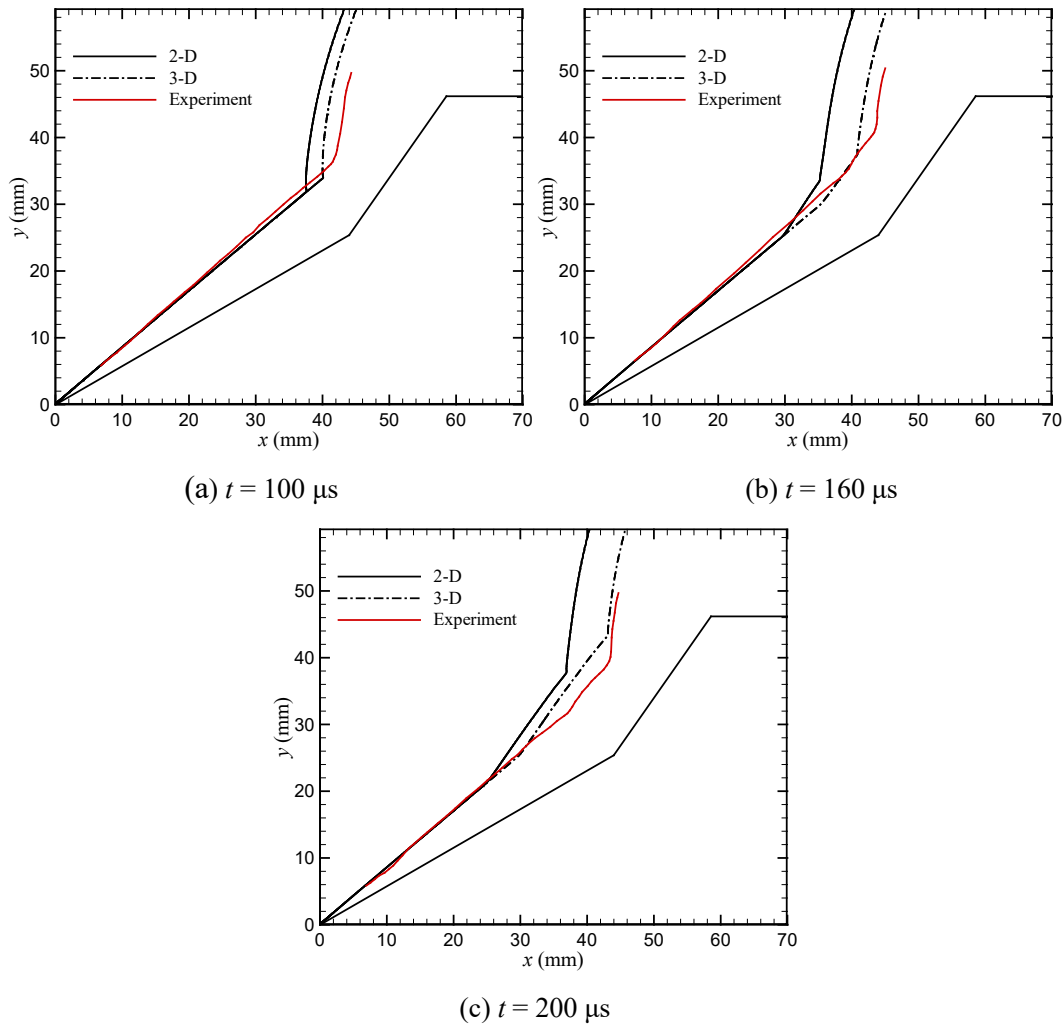
Fig. 12. Comparison of experimental and simulated shock shapes at different instants in

nitrogen.

Figure 13 presents the experimental schlieren images [41] and simulated density gradient contours at different instants. Since no schlieren images were provided beyond $t = 200$ μs, the comparison is made at $t = 60$, 120, and 180 μs. Note that only the results obtained from the 3-D simulation are shown. As seen from the figure, the shock interaction mechanisms observed in the experiments can be well reproduced by the numerical simulation. Good agreement is obtained in terms of the shock shape, the location of the triple point, the separation and reattachment shocks, and the slip lines.

(a) $t = 60$ μs

(b) $t = 120$ μs

(c) $t = 180$ μs
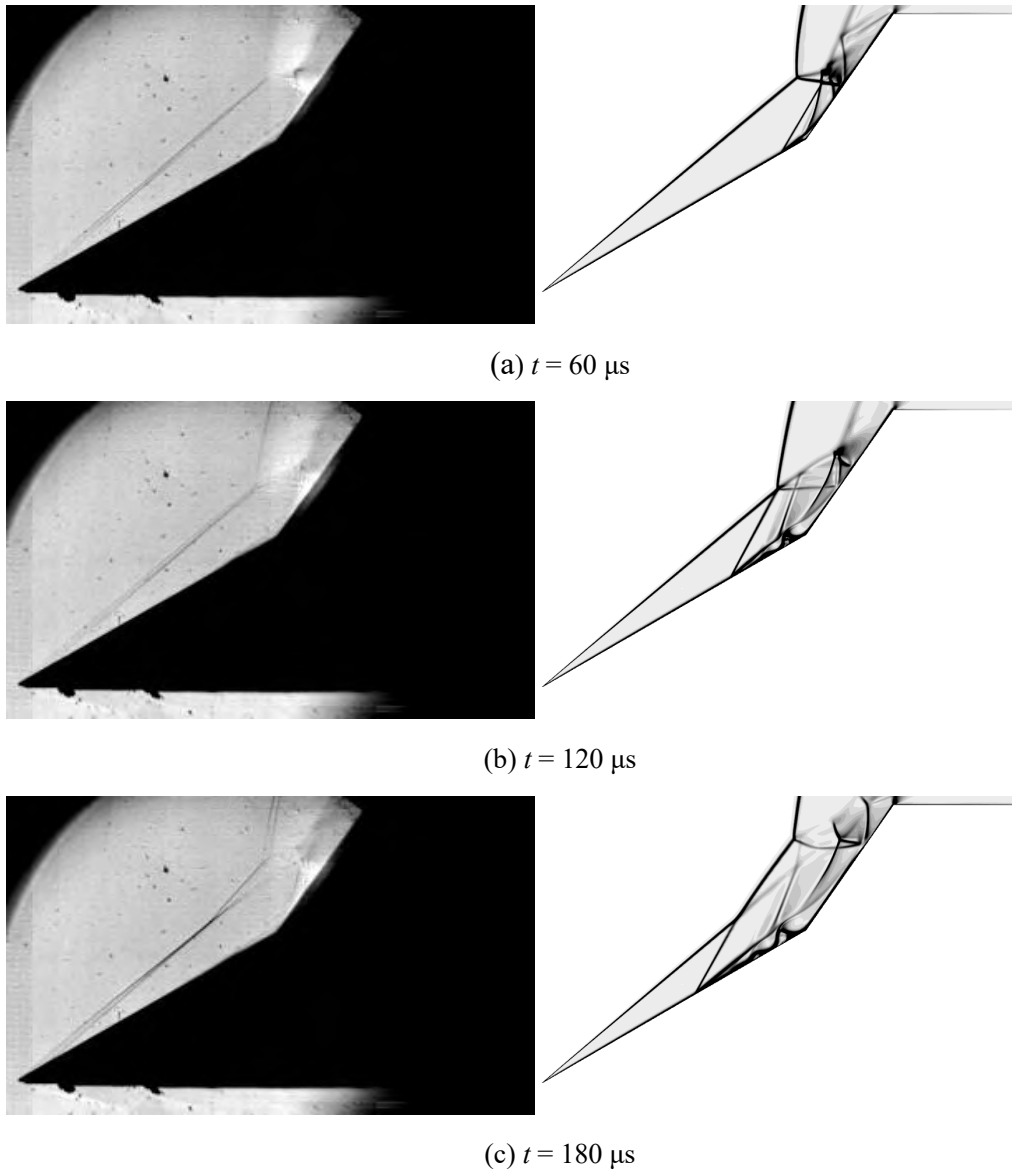
Fig. 13. Comparison of experimental schlieren images [41] (left) and density gradient contours at the midspan obtained from the 3-D simulation (right) at different instants in nitrogen. Reprinted with permission from A. Swantek.

Figure 14 presents the simulated surface heat flux averaged from $t = 100$ to 242 μs with the measurements. Note that the multiple-measured heat fluxes at the same streamwise location correspond to different shots [8]. It is observed that the numerical results and the experimental data are in reasonably close agreement. Although the separation points are different between the 2-D and 3-D simulations, they both can match the experimental results well near $x = 20$ mm. Additionally, it seems that both the 2-D and 3-D peak values could fall within the measurement uncertainty. An evident disagreement between the numerical predictions and the experimental data occurs near

$x = 50$ mm. In the experiment, the time-averaged heat flux at this location is nearly as large as the peak value, which is not observed from the numerical simulations. The discrepancy could be attributed to the inaccurate modeling of the tunnel start-up process according to Knight et al. [13].
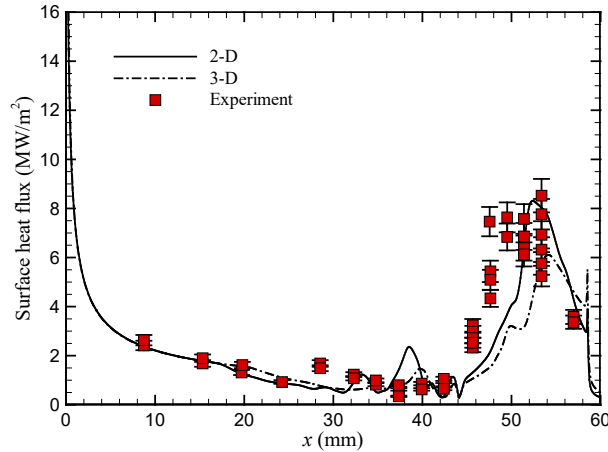

Fig. 14. Comparison of experimental and simulated time-averaged surface heat flux in nitrogen.

6 Results and discussion: air flow

6.1 Shock interaction mechanisms

Contours of the density gradient magnitude obtained from the 2-D simulation are displayed in Fig. 15 at $t = 60$, 120, 180, and 242 μs for the air flow. At $t = 60$ μs, the separation bubble is relatively small so that the separation and reattachment shocks interact with each other before they meet the TS induced by the AS and DS generated by the first and second wedges, respectively. Edney's type I interaction can be observed. The shocks are then reflected by the SL and the wedge surface. From $t = 120$ to 242 μs, as the separation bubble grows, the separation point moves upstream, whereas the reattachment point moves downstream. During the process, the overall shock interaction mechanisms remain unchanged. Compared with the 2-D results for the nitrogen flow, the standoff distance of the BS and the size of the separation region are smaller. In fact, the real-gas effects tend to reduce the post-shock temperature and thus increase the post-shock density relative to the nitrogen results, leading to a decrease in the shock standoff distance. As discussed in Ref. [42], the same changes occur in the separation region resulting in a reduced separation bubble. Additionally, the 2-D

simulation has not reached steady state at $t = 242$ μs.

(a) $t = 60$ μs

(b) $t = 120$ μs

(c) $t = 180$ μs

(d) $t = 242$ μs
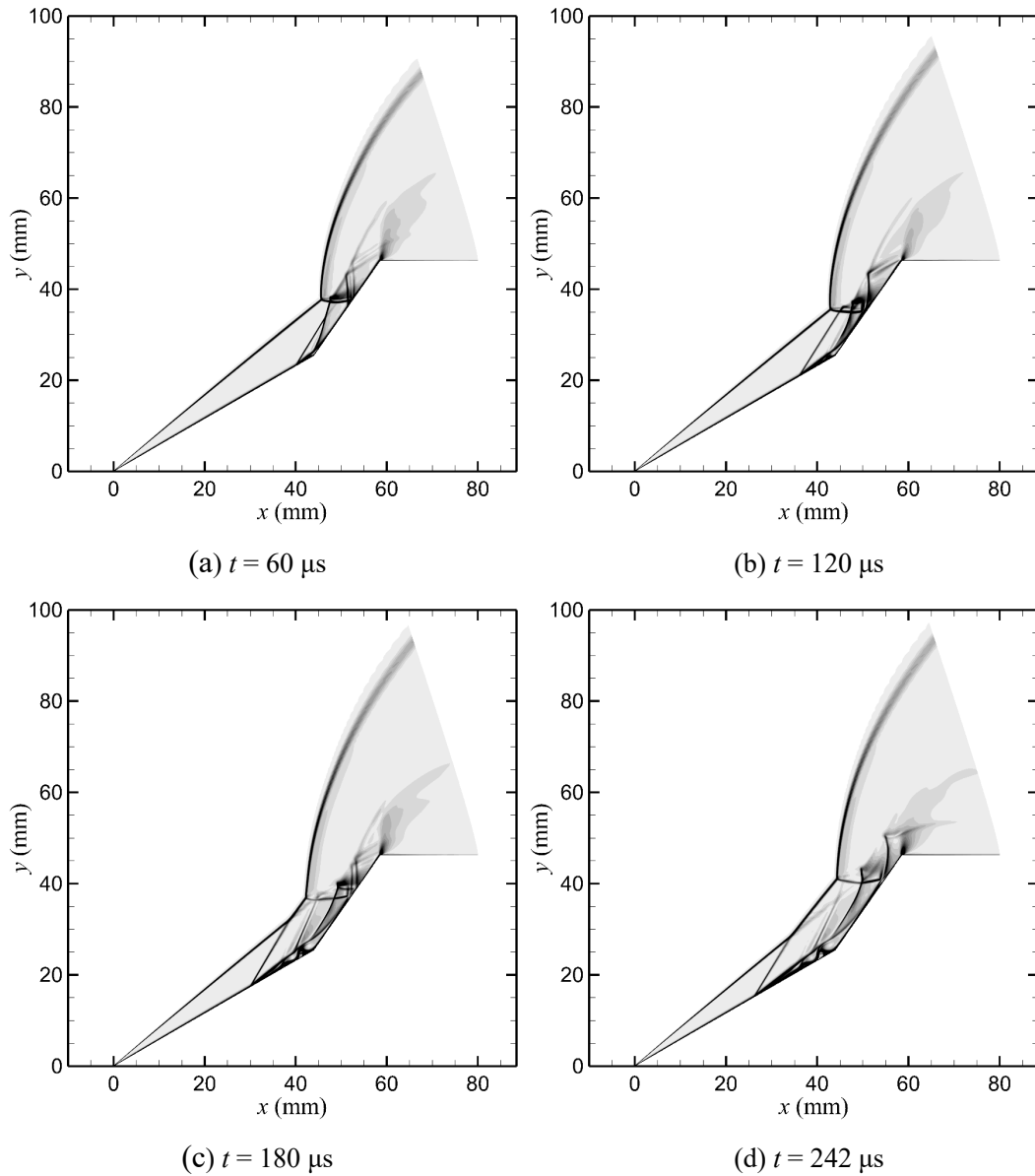
Fig. 15. Contours of the density gradient magnitude obtained from the 2-D simulation at different instants in air.

Figures 16–18 show the evolutions of surface skin friction, heat flux, and pressure obtained from the 2-D simulation, respectively. The variation trend is in accordance with the description of the 2-D nitrogen simulation. Note that the peak heat flux at different instants is lower than that in nitrogen. This is because the real-gas effects result in a smaller separation region and thus a weaker shock interaction. Similar effects have been demonstrated by previous studies [4,42] on high-enthalpy double-cone flows.
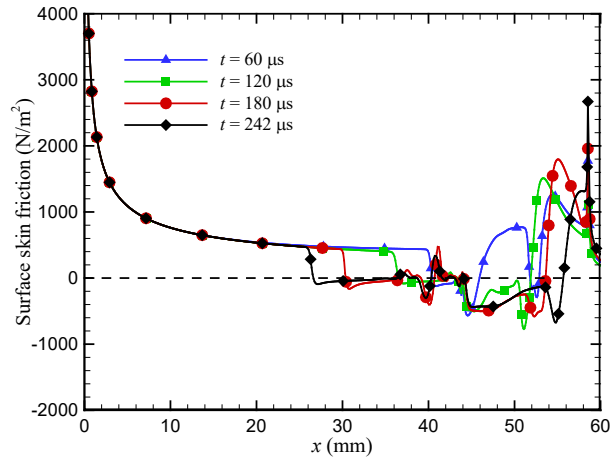
**Fig. 16. Evolutions of surface skin friction obtained from the 2-D simulation in air.**
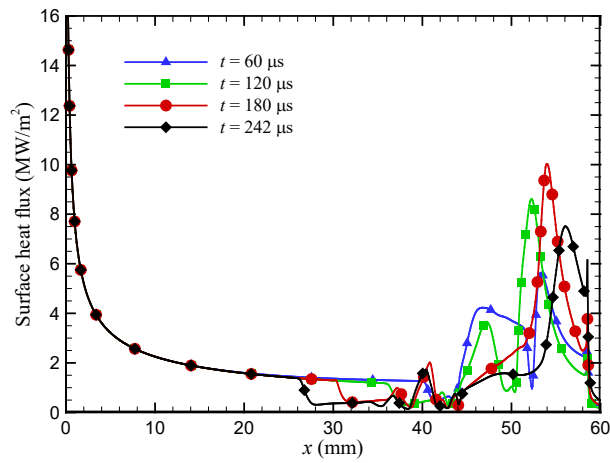
**Fig. 17. Evolutions of surface heat flux obtained from the 2-D simulation in air.**
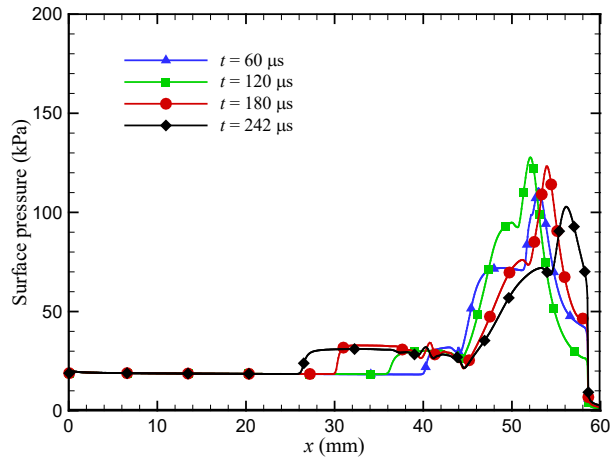
Fig. 18. Evolutions of surface pressure obtained from the 2-D simulation in air.

6.2 Comparison with experiments

Figure 19 shows the experimental and simulated shock shapes at different instants. Good agreement is obtained, indicating that the air flow over the double-wedge configuration can be well described by the 2-D assumption.

(a) $t = 60$ μs

(b) $t = 120$ μs

(c) $t = 200$ μs
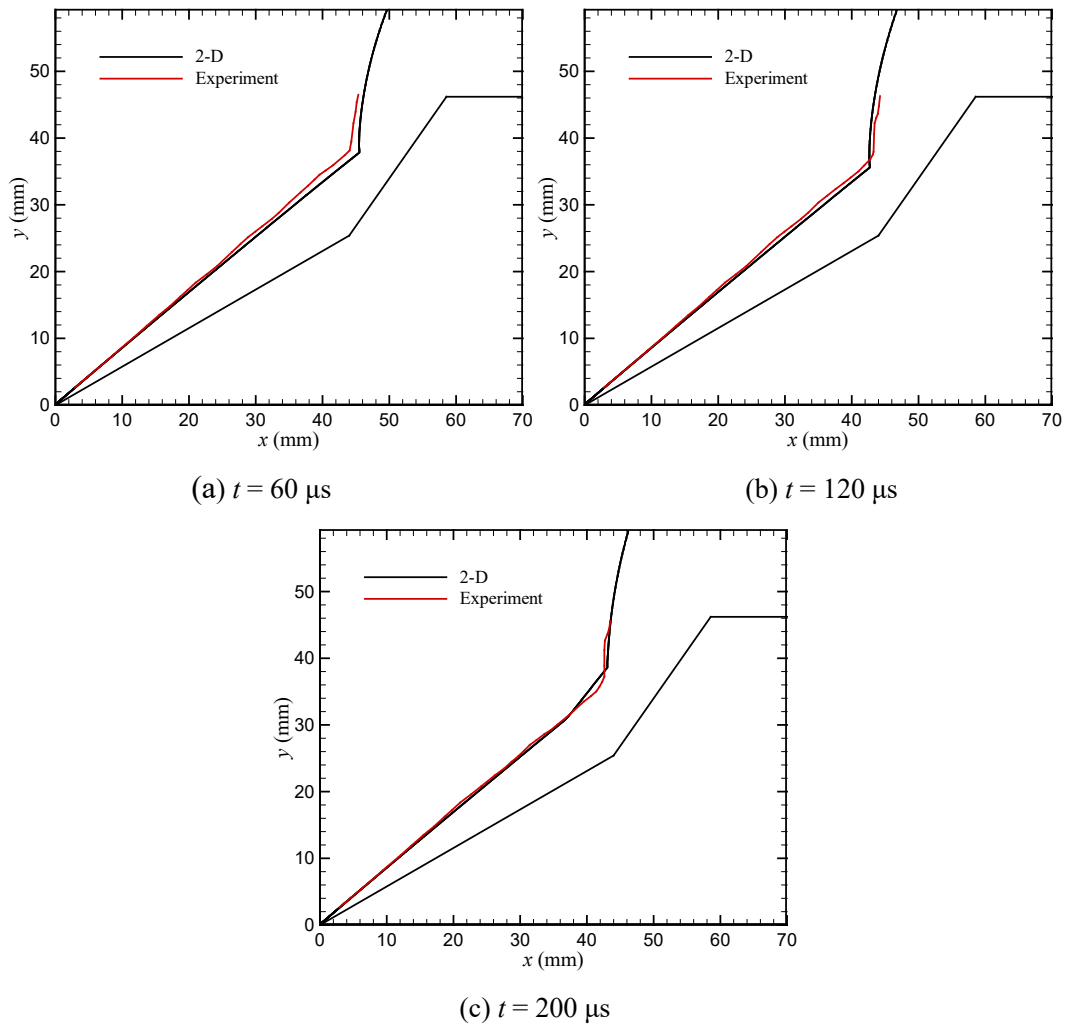
Fig. 19. Comparison of experimental and simulated shock shapes at different instants in air.

Figure 20 shows the experimental schlieren images [41] and simulated density gradient contours at different instants. Due to the flow luminescence, the flow structure in the interaction region cannot be identified clearly. Nevertheless, the shock shape, the location of the triple point, and the transmitted and reattachment shocks are accurately captured by the numerical simulation.

(a) $t = 60$ μs

(b) $t = 120$ μs

(c) $t = 180$ μs
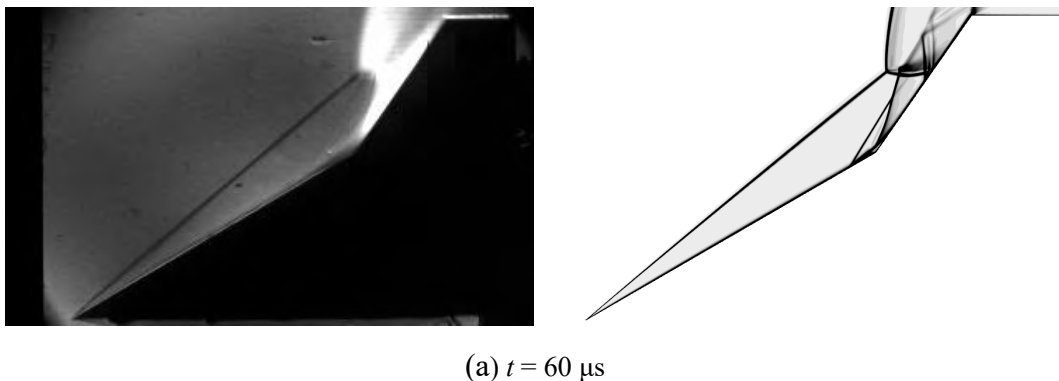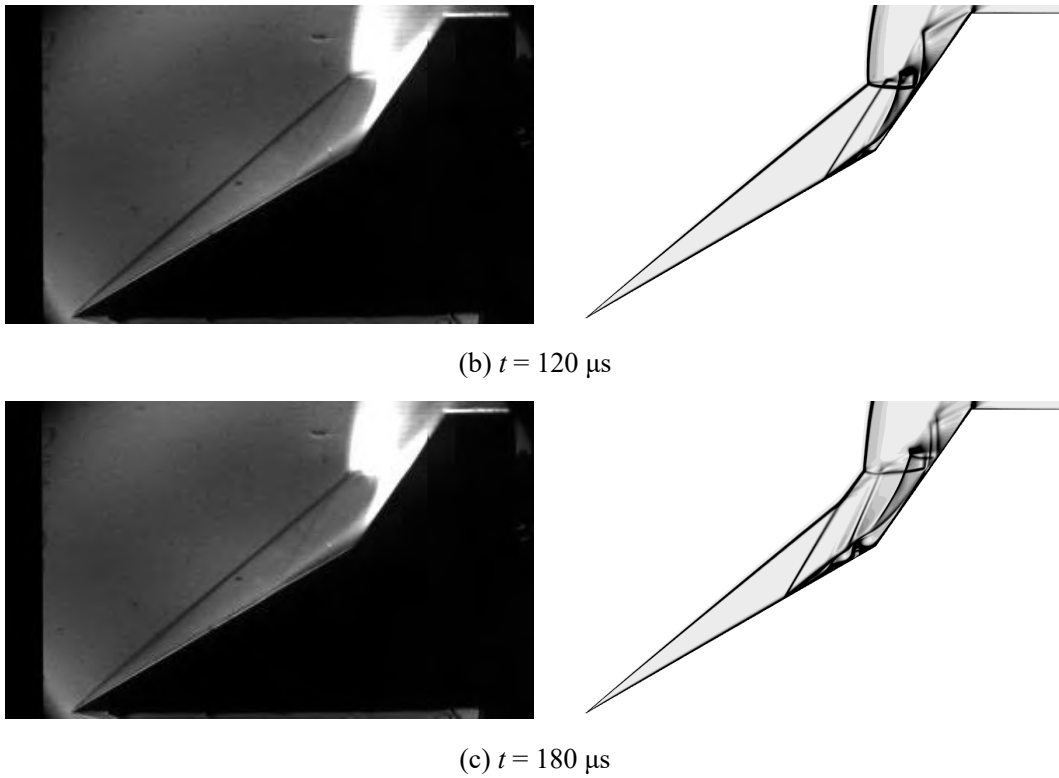
Fig. 20. Comparison of experimental schlieren images [41] (left) and computed density gradient contours obtained from the 2-D simulation (right) at different instants in air. Reprinted with permission from A. Swantek.

Figure 21 shows the experimental and simulated time-averaged surface heat flux. Good agreement is obtained between the experiment and computation upstream of the predicted separation point. The location of the peak value also agrees well with the experimental data. However, there are two major discrepancies: the predicted separation point seems to be ahead of the measurement; the heat flux between $x = 46$ and 54 mm is significantly underestimated by the numerical simulation.
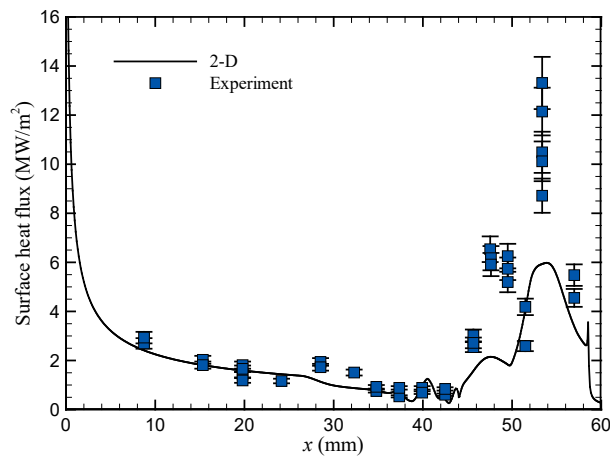

Fig. 21. Comparison of experimental and simulated time-averaged surface heat flux in air.

In general, the real gas effects on the double-wedge flow can be summarized as follows: A large amount of the translational energy of the gas is absorbed by the vibrational excitation and dissociation of molecular oxygen behind the bow shock. As a result, the post-shock translational temperature is much lower than its nonreactive counterpart. Since the pressure is largely unchanged, the post-shock mixture density increases, leading to a smaller shock standoff distance and thus a weaker shock interaction strength and a lower heat flux peak. The denser gas behind the detached shock is redirected into the separation region, causing a reduced separation bubble.

6.3 Effect of thermochemical nonequilibrium models

To understand the discrepancies in the surface heat flux for the air flow between the numerical simulation and the experimental data, effects of thermochemical nonequilibrium models are investigated in this section by simulating the air flow case using the improved scheme. As seen in Fig. 22, the difference in the distributions predicted by the baseline and improved schemes are slight, indicating that the double-wedge flow in air under the current condition is insensitive to air chemistry and vibration–dissociation coupling models. In fact, the experimental freestream condition is moderate due to the relatively low total enthalpy (8.0 MJ/kg), leading to low post-shock temperatures and thus weak vibrational excitation and chemical reactions.
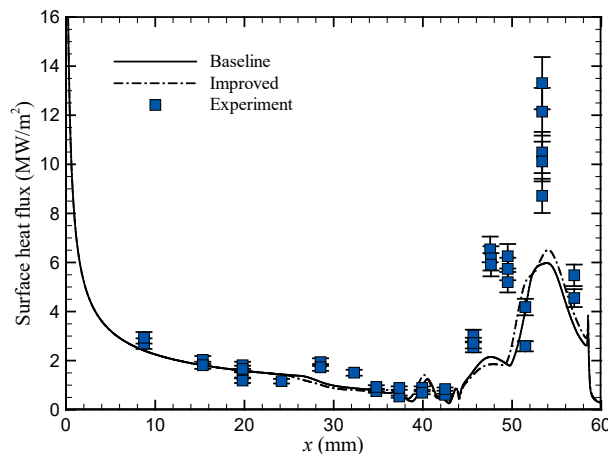
Fig. 22. Comparison of time-averaged surface heat flux predicted by the baseline and improved models in air.

Figure 23 shows the contours of T_{tr} predicted using the baseline and improved schemes at $t = 242$ μs. As seen in the figure, the peak value in T_{tr} (approximately 7500

K) occurs immediately behind the detached shock near the triple point. The flow structures predicted by the two schemes are nearly identical. The relatively low post-shock T_{tr} is unable to trigger substantial dissociation reactions. At $t = 242$ μs, the largest mass fraction of atomic O is around 0.15, as shown in Fig. 24.
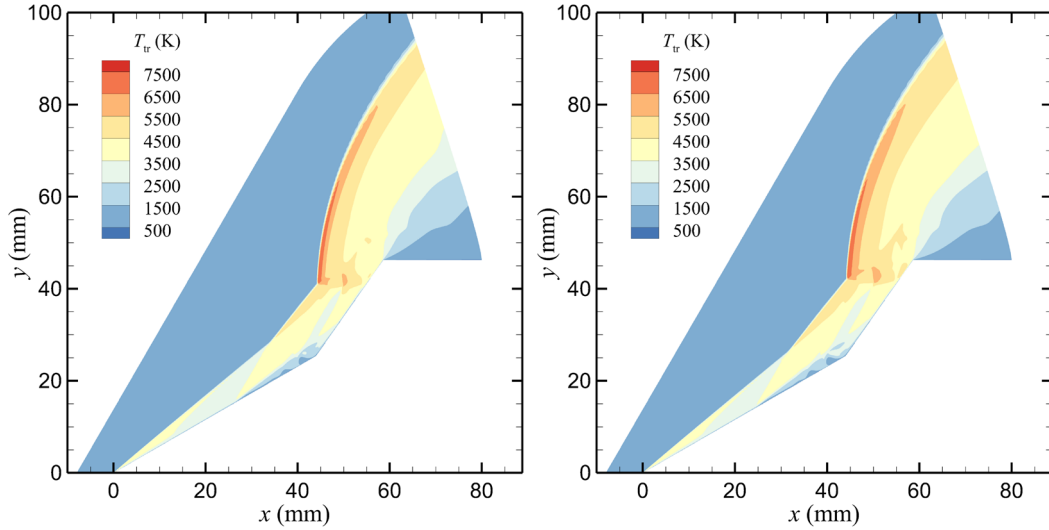

Fig. 23. Contours of the translational–rotational temperature predicted by the baseline (left) and improved (right) models at $t = 242$ μs in air.
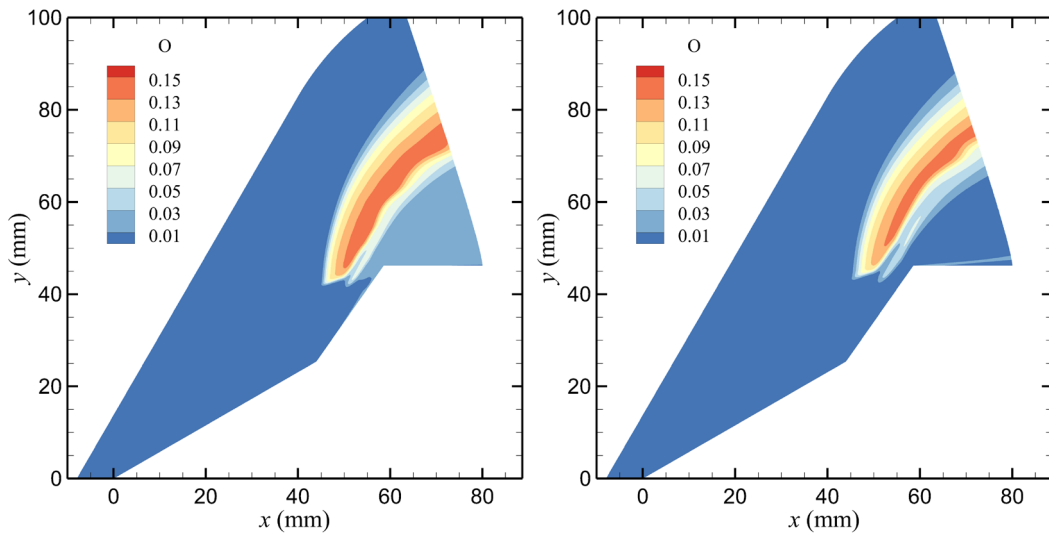

Fig. 24. Contours of the mass fraction of atomic O predicted by the baseline (left) and improved (right) models at $t = 242$ μs in air.

The comparison indicates that the air flow is insensitive to thermochemical nonequilibrium models and that the experiment can only partially represent a test of nonequilibrium effects given the evident difference between the air and nitrogen flows. However, there is a notable disagreement between the numerical predictions and the

experimental data. Figure 25 shows the experimental and simulated time-averaged heat flux distributions for the nitrogen and air flows in a single frame. Due to the real-gas effects described in Section 6.1, the predicted peak heat flux is lower in air than in nitrogen. However, the trend in the experiments shows the opposite indicating that attributing the difference between the nitrogen and air flows to the real gas effects could be simplistic. There might be other sources of the disagreement such as potential laminar-turbulent transition suggested by Pezzella et al. [43] and modeling of the tunnel startup process in short-duration test facilities suggested by Knight et al. [13]. In this paper, only the effect of transition is preliminarily studied.
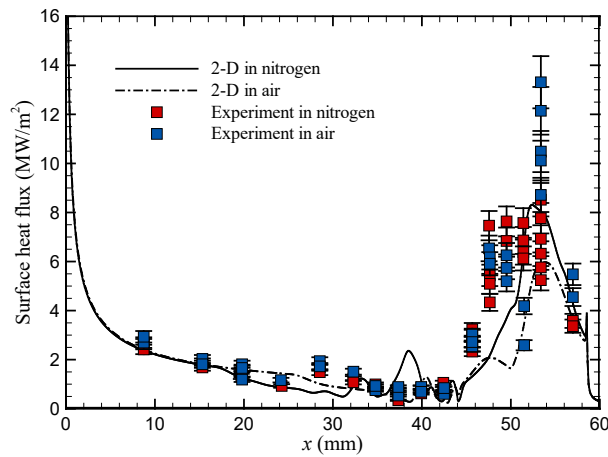

Fig. 25. Time-averaged surface heat flux in nitrogen and air.

6.4 Effect of Laminar-Turbulent Transition

Due to the instability of the shear layers, perturbations could be formed and affect the flow structure, leading to possible local laminar-turbulent transition [44]. Furthermore, previous direct numerical simulations [45,46] have shown that real-gas effects tend to destabilize Mack's second mode, which dominates the transition process at high Mach numbers. Therefore, the air flow could be more vulnerable to instabilities than the nitrogen flow. In this section, two additional simulations are performed with transition to turbulence at $x = 0.58L_1$ and L_1, respectively. These locations are the same with those used by Pezzella et al. [43]. As a preliminary study, a compressible form of Spalart–Allmaras one-equation model [47] is used for turbulence modeling. Figure 26 shows the fully laminar and transitional time-averaged surface heat flux for the air flow. The effects of transition to turbulence at $x = L_1$ are to move the separation point

downstream and increase the peak heat flux, better matching the experimental data. Similar trend was also reported by Pezzella et al. [43] and Knight et al. [13]. These results indicated that the potential laminar-turbulent transition in local regions of the air flow should be studied in more detail in the future.
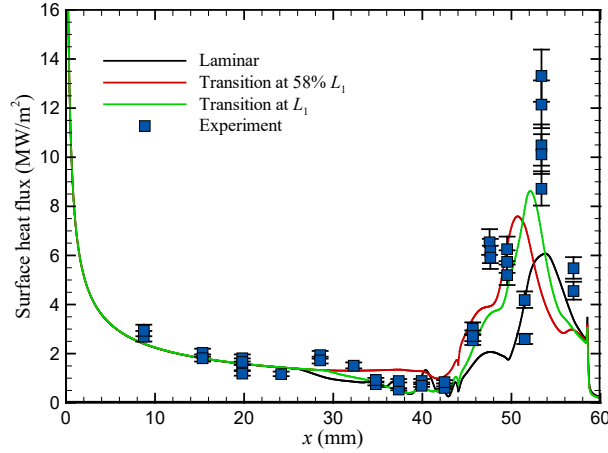

Fig. 26. Comparison of laminar and transitional time-averaged surface heat flux in air.

7 Conclusions

Hypersonic flows over a double-wedge configuration in nitrogen and air are numerically investigated with total enthalpy of 8.0 MJ/kg. Time-accurate 2-D and 3-D simulations are performed using a multi-block finite-volume CFD code to reveal the unsteady shock interaction mechanisms.

For the nitrogen flow, it is found that both the 2-D and 3-D simulations have not researched steady states at the end of the test time. During the developing process, the separation and reattachment points move upstream and downstream, respectively. The locations of the heat flux and pressure peaks also move downstream consequently. The three-dimensional simulation predicts a much smaller separation bubble and reduced peak surface heat flux and pressure. Good agreement can be observed with the experiments in terms of the shock shape, the flow structure, and the time-averaged surface heat flux when the three-dimensional effects are considered. However, it is important to note that the current 3-D unsteady simulation is initialized without any perturbation. Therefore, the 3-D effect discussed in this paper mainly corresponds to flow relieving. The potential Görtler instabilities near reattachment and intrinsic instabilities of the separation bubble unobserved here due to the short simulation time

should be addressed in a future study.

For the air flow, the shock interaction mechanisms are similar to those in nitrogen. The real-gas effects tend to decrease the separation bubble and reduce the standoff distance of the detached shock induced by the second wedge, leading to a lower surface heat flux near the impingement point compared with the nitrogen result. However, the trend of the experimental heat flux data shows the opposite. To explain the discrepancies, an additional simulation is performed using the improved scheme, which accounts for the upgraded air chemistry and vibration–dissociation coupling models. The results indicate that the air flow under the current condition is insensitive to thermochemical nonequilibrium models. The conclusion is not surprising due to the relatively low total enthalpy. It can be inferred that the discrepancies are caused by other sources. Specifically, a preliminary study on the effects of transition to turbulence is performed. Transition at $x = L_1$ shifts the separation point downstream and increases the peak heat flux, better matching the experimental data. It is suggested that modeling of the tunnel start-up process and laminar-turbulent transition in local regions require further investigation.

Acknowledgements

References

[1] J. D. Anderson, Jr., Hypersonic and high-temperature gas dynamics, 2nd ed., AIAA, Reston, 2006.

[2] K. J. Weilmuenster, P. A. Gnoffo, F. A. Greene, Navier–Stokes simulations of orbiter aerodynamic characteristics including pitch trim and bodyflap, J. Spacecraft and Rockets, 31(3) (1994) 355–366.

[3] M. S. Holden, T. P. Wadhams, M. Maclean, Experimental studies in the LENS

supersonic and hypersonic tunnels for hypervelocity vehicle performance and code validation, AIAA 2008–2505, 2008.

[4] M. S. Holden, T. P. Wadhams, M. Maclean, A. Dufrene, Experimental research and analysis in supersonic and hypervelocity flows in the LENS shock tunnels and expansion tunnel, AIAA 2015–3660, 2015.

[5] C. Y. Wen, H. G. Hornung, Non-equilibrium dissociating flow over spheres, Journal of Fluid Mechanics, 299 (1995), 389–405.

[6] C. Y. Wen, H. Saldívar Massimi, H. Shen, Extension of CE/SE method to non-equilibrium dissociating flows, Journal of Computational Physics, 356 (2018), 240–260.

[7] H. Shen, C. Y., Wen, Theoretical investigation of shock stand-off distance for non-equilibrium flows over spheres, Chinese Journal of Aeronautics, in press, Feb. 18, 2018.

[8] A. B. Swantek, J. M. Austin, Heat transfer on a double wedge geometry in hypervelocity air and nitrogen flows, AIAA 2012–0284, 2012.

[9] A. S. Durna, M. A. Barada, B. Celik, Shock interaction mechanisms on a double wedge at Mach 7, Physics of Fluids, 28 (2016) 096101.

[10] J. R. Komives, I. Nompelis, G. V. Candler, Numerical investigation of unsteady heat transfer on a double wedge geometry in hypervelocity flows, AIAA 2014–2354, 2014.

[11] J. D. Reinert, S. GS, G. V. Candler, Three-dimensional simulations of hypersonic double wedge flow experiments, AIAA 2017–4125, 2017.

[12] O. Tumuklu, D. A. Levin, J. M. Austin, Shock-shock interactions for a double wedge configuration in different gases, AIAA 2015–1520, 2015.

[13] D. Knight, O. Chazot, J. Austin, M. A. Badr, G. Candler, B. Celik, D. de Rosa, R. Donelli, J. Komives, A. Lani, D. Levin, I. Nompelis, M. Panesi, G. Pezzella, B. Reimann, O. Tumuklu, K. Yuceil, Assessment of predictive capabilities for aerodynamic heating in hypersonic flow, Progress in Aerospace Sciences, 90 (2017) 39–53.

[14] N. Kianvashrad, D. Knight, Simulation of hypersonic shock-wave–laminar-

boundary-layer interaction on hollow cylinder flare, AIAA J., 55(1) (2017) 322–326.

[15] A. B. Swantek, J. M. Austin, Flowfield Establishment in Hypervelocity Shock-Wave/Boundary-Layer Interactions, AIAA J., 53(2) (2015) 311–320.

[16] C. Park, Nonequilibrium hypersonic aerothermodynamics, Wiley, New York, 1990.

[17] W. G. Vincenti, C. H. Kruger, Introduction to physical gas dynamics, Krieger, Malabar, 1965.

[18] R. C. Millikan, D. R. White, Systematics of vibrational relaxation, J. Chemical Physics, 39(12) (1963) 3209–3213.

[19] D. Hash, J. Olejniczak, M. Wright, D. Prabhu, M. Pulsonetti, B. Hollis, P. Gnoffo, M. Barnhardt, I. Nompelis, G. Candler, FIRE II calculations for hypersonic nonequilibrium aerothermodynamics code verification: DPLR, LAURA, and US3D, AIAA 2007–0605, 2007.

[20] P. A. Gnoffo, R. N. Gupta, J. L. Shinn, Conservation equations and physical models for hypersonic air flows in thermal and chemical nonequilibrium, NASA TP-2867, 1989.

[21] D. A. Andrienko, I. D. Boyd, Rovibrational energy transfer and dissociation in O_2–O collisions, The J. of Chemical Physics, 144 (2016) 104301.

[22] D. A. Andrienko, I. D. Boyd, State-resolved O_2–N_2 kinetic model at hypersonic temperatures, AIAA Paper 2017–0659, 2017.

[23] D. A. Andrienko, I. D. Boyd, State-specific dissociation in O_2–O_2 collisions by quasiclassical trajectory method, Chemical Physics, 491 (2017) 74–81.

[24] P. V. Marrone, C. E. Treanor, Chemical relaxation with preferential dissociation from excited vibrational levels, Physics of Fluids, 6(9) (1963) 1215–1221.

[25] M. Lino da Silva, V. Guerra, J. Loureiro, Two-temperature models for nitrogen dissociation, Chemical Physics, 342 (2007) 275−287.

[26] J. Hao, J. Wang, C. Lee, Assessment of vibration–dissociation coupling models for hypersonic nonequilibrium simulations, Aerospace Science and Technology 67 (2017) 433–442.

[27] K. Sutton, P. A. Gnoffo, Multi-component diffusion with application to

computational aerothermodynamics, AIAA 1998–2575, 1998.

[28] R. N. Gupta, J. M. Yos, R. A. Thompson, K. P. Lee, A review of reaction and thermodynamic and transport properties for an 11-species air model for chemical and thermal nonequilibrium calculations to 30 000 K, NASA RP-1232, 1990.

[29] M. J. Wright, D. Bose, G. E. Palmer, Eugene Levin, Recommended collision integrals for transport property computations, part 1: air species, AIAA J., 43(12) (2005) 2558–2564.

[30] J. Hao, J. Wang, C. Lee, Numerical study of hypersonic flows over reentry configurations with different chemical nonequilibrium models, Acta Astronautica, 126 (2016) 1–10.

[31] J. Hao, J. Wang, C. Lee, Development of a Navier–Stokes code for hypersonic nonequilibrium simulations, AIAA 2017–2164, 2017.

[32] J. Hao, J. Wang, C. Lee, Numerical simulation of high-enthalpy double-cone flows, AIAA J., 55(7) (2017) 2471–2475.

[33] J. Hao, J. Wang, C. Lee, Numerical simulation of high-enthalpy hollow-cylinder flare flows, AIAA J., 56(8) (2018) 3337–3341.

[34] J. Hao, C. Y. Wen, Numerical investigation of oxygen thermochemical nonequilibrium on high-enthalpy double-cone flows, International Journal of Heat and Mass Transfer, 127 (2018) 892–902.

[35] J. Hao, C. Y. Wen, Effects of vibrational nonequilibrium on hypersonic shock-wave/laminar boundary-layer interactions, International Communications in Heat and Mass Transfer, 97 (2018) 136–142.

[36] R. W. MacCormack, Numerical computation of compressible and viscous flow, AIAA, Reston, 2014.

[37] B. van Leer, Towards the ultimate conservative difference scheme, J. Computational Physics, 32(1) (1979) 101–136.

[38] E. F. Toro, Riemann solvers and numerical methods for fluid dynamics a practical introduction, Springer, Berlin, 1997.

[39] D. M. Peterson, Simulations of injection, mixing, and combustion in supersonic flow using a hybrid RANS/LES approach, University of Minnesota, 2011.

[40] B. E. Edney, Effects of shock impingement on the heat transfer around blunt bodies, AIAA J., 6(1) (1968) 15–21.

[41] A. Swantek, The role of aerothermochemistry in double cone and double wedge flows, University of Illinois at Urbana-Champaign, 2012.

[42] H. Babinsky, J. K. Harvey, Shock wave–boundary-layer interactions, Cambridge University Press, New York, 2011.

[43] G. Pezzella, D. de Rosa, R. S. Donelli, Computational analysis of shock wave boundary layer interactions in non-equilibrium hypersonic flow, AIAA 2015–3578, 2015.

[44] G. Shoev, G. Oblapenko, O. Kunova, M. Mekhonoshina, E. Kustova, Validation of vibration-dissociation coupling models in hypersonic non-equilibrium separated flows, Acta Astronautica, 144 (2018) 147–159.

[45] Y. Ma, X. Zhong, Receptivity to freestream disturbances of a Mach 10 nonequilibrium reacting oxygen flow over a flat plate, AIAA 2004–0256, 2004.

[46] X. Zhong, X. Wang, Direct numerical simulation on the receptivity, instability, and transition of hypersonic boundary layers, Annual Review of Fluid Mechanics, 44 (2012) 527–561.

[47] S. Catris, B. Aupoix, Density corrections for turbulence models, Aerospace Science and Technology, 4(1) (2000) 1–11.